We are IntechOpen, the world's leading publisher of Open Access books Built by scientists, for scientists

4,800
Open access books available

122,000
International authors and editors

135M
Downloads

Our authors are among the

154
Countries delivered to

TOP 1%
most cited scientists

12.2%
Contributors from top 500 universities

WEB OF SCIENCE™

Selection of our books indexed in the Book Citation Index
in Web of Science™ Core Collection (BKCI)

Interested in publishing with us?
Contact book.department@intechopen.com

Numbers displayed above are based on latest data collected.
For more information visit www.intechopen.com

Mechanics of Electric Rope Shovel Performance and Reliability in Formation Excavation

Muhammad Azeem Raza and Samuel Frimpong

Additional information is available at the end of the chapter

Abstract

Large-capacity rope shovels are used as primary production equipment in many surface mining operations. Current rope shovels have payload capacities in excess of 100 tons per pass. The dynamic payload and formation resistive forces result in severe stress loading of the shovel front-end assembly. Material flaws, high stresses, and harsh excavation conditions can initiate cracks in the dipper-teeth assembly. These cracks, under high stresses, can propagate to critical lengths resulting in fatigue failure of front-end assembly. Dipper-related problems can significantly reduce shovel availability. There is no fundamental research for understanding dipper fatigue failure resulting from high stress intensity, crack initiation, and propagation, the subject matter of this study. The Newton-Euler algorithm is used to build kinematics and dynamic models of the cable shovel front-end assembly. The models incorporate the dynamic resistive forces on the dipper-teeth assembly. Numerical simulations are used to generate the dynamic payload force and its dynamic left. Virtual simulation, based on the P&H 4100XPC shovel prototype in ANSYS (R15), is run to generate stress loading of the dipper-teeth assembly and equivalent (von Mises) stresses. Stress intensity factors are computed for various crack lengths in the dipper-teeth assembly, and the crack-propagation lives are computed for these cracks. The results show that a 75-mm crack can propagate to the critical length in 16 days. This research study provides a pioneering effort toward understanding shovel dipper fatigue failure due to high stress intensity, crack initiation, and propagation for understanding shovel reliability and availability for production efficiency and bulk production economics.

Keywords: formation excavation, machine kinematics and dynamics, virtual simulation, stress profile intensity

1. Introduction

Cable shovels are used as primary excavation equipment in large-scale surface mining operations. The overall efficiency of shovel-truck surface mining operations is largely dependent on shovel efficiency. Dipper payloads of the shovels have seen an increasing trend over the years, and current shovels have payloads in excess of 100 tons per scoop [1, 2]. The payloads, combined with dipper weight, rigging, and variable material diggability, result in varying mechanical energy inputs and stress loading of the shovel's front-end assembly across the working bench. Furthermore, the repeated shovel loading and unloading cycles induce fatigue stresses in shovel components. The induced stresses over time may exceed the yield strength of steel/material of the shovel leading to fatigue failure, teeth losses, and boom and handle cracks. High stresses and fatigue failure in shovel front-end assembly cause unplanned downtimes resulting in reduced efficiency and increased production costs. Dipper-related problem can be a significant contributor to the shovel downtime [3]. The current practice for the shovel front-end assembly repair is based on experience and history rather than science.

Electric rope shovel consists of the lower, upper, and the front-end assembly as illustrated in **Figure 1**. The lower assembly consists of the propel drive and crawler systems and provides a solid and stable base for the excavator. This helps excavator propel, reposition, and relocation during its operation.
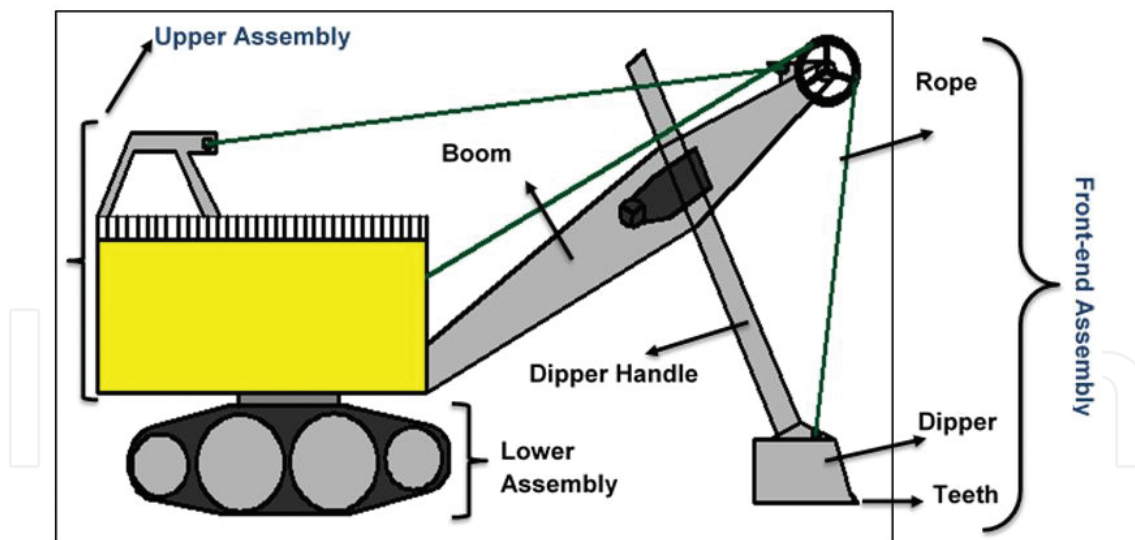

Figure 1. Nomenclature of a cable shovel.

The shovel's upper assembly is a roller and left-pin system mounted on the lower mechanism. The upper assembly consists of multiple decks with housing for the hoist and swing machinery and electronic control cabinet on the lower deck and the operator's cab on the upper deck. Additionally, the upper assembly provides a platform for boom attachment and the counter weight for the dipper. The front end consists of the boom, crowd machinery, dipper handle,

dipper, and ropes. During the normal duty cycle, the shovel stays at one position, and only the front end engages with the formation.

2. Shovel resistance forces and modeling

The dipper excavation processes can be categorized into penetration, cutting, and scooping processes [4, 5]. Penetration is the insertion of a tool into a medium, and cutting is the lateral movement of a tool, executed at a constant depth. The dipper teeth penetrate the formation, and the lip cuts the material. Excavation models are based on the formation resistive forces acting on the cutting tool. The resistive forces combine the cutting forces at the dipper teeth and lip and the excavation forces due to material movement along, ahead, and inside the dipper. Both the experimental and analytical models are based on these resistive forces. The model proposed by Hemami [6] is by far the most comprehensive model and consists of six component forces (f_1 to f_6), which must be overcome during excavation, as in **Figure 2**. All these forces, except f_6, are dynamic forces. The six forces acting on the dipper, from the initial to the end point on trajectory, consist of the following:

f_1: The force required to overcome the payload weight in and above the dipper

f_2: The resultant resistive force due to material movement toward the dipper

f_3: The friction force between the bucket walls and the excavated material as it slides into the dipper

f_4: The resistance to cutting and/or penetrating that acts at the dipper tip and side walls

f_5: The inertia force of the material inside and above the dipper

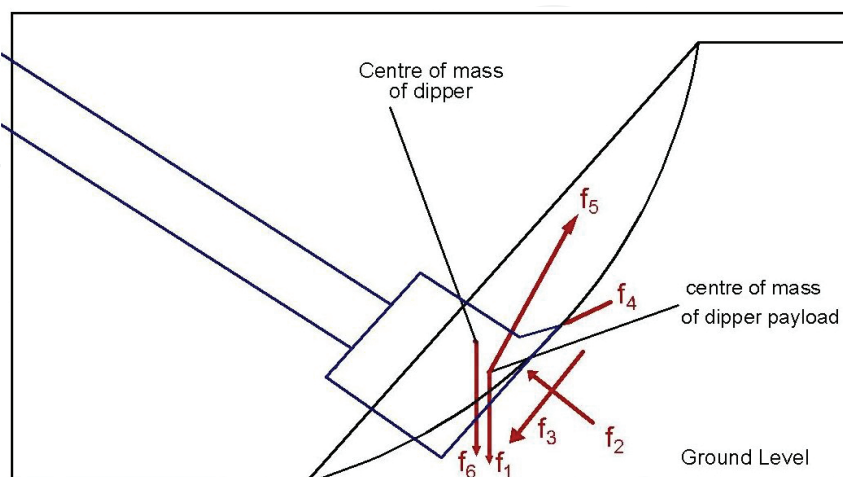f_6: The force required to move the empty dipper (modeled as part of f_1)

Figure 2. Forces on a dipper during excavation [7].

The forces, f_1 and f_5, are the dynamic forces [7], where f_1 changes both in magnitude and the point of application, and f_5 depends on the bucket acceleration. The force (f_6) was originally defined as a part of f_1 and f_5. The dipper payload force (f_1) is the dominant force for the large-capacity dippers [6, 8, 9]. Awuah-Offei et al. [8] proposed a model based on the Balovnev [10] excavation model using the six forces. The force (f_2) can be set to zero [6]. Forces, f_3 and f_4, are the cutting forces and can be combined as a single force and estimated using the empirical model [11] given by Eq. (1).

This empirical model is a result of extensive experimentation on frozen soils [11]. z is the coefficient that accounts for the blade impact on cutting force, which depends on w and d. **Table 1** is used to estimate z for d (between 25 cm and 50 cm). z increases as d decreases, and it also depends on the ratio T_s/T_w (T_s is the spacing between the teeth, and T_w is the tooth width). **Table 2** lists the multiplying factors for z based on T_s/T_w. Force f_5 can also be set to zero if the dipper moves with a uniform velocity through the muck pile. Force f_6 can be modeled as part of f_1:

Length of horizontal surface (w, m)	0.25–0.50	0.50–0.75	0.75–1.00	1.00–1.25
Coefficient z	0.55–0.75	0.63–0.78	0.69–0.8	0.71–0.82

Table 1. Dependence of "z" on "d," and "w".

Ratio T_s/T_w	$T_s = T_w$	$T_s = 2T_w–3T_w$	$T_s = 4T_w$	$T_s = 5T_w$
z	1.2	1	1.1	1.25

Table 2. Dependence of z on T_s/T_w [11].

$$P=10C_o\ d^{1.35}\ (1+2.6w)(1+0.0075\beta')z \tag{1}$$

3. Kinematic model of the cable shovel front end

A kinematic model of the shovel is required to completely describe the motions (accelerations, velocities, and displacements). The kinematic model further provides a basis for the dynamic model, which can be used to calculate the torques and forces on individual components. The complete shovel digging process involves propel, crowd, and swing motions. However, during the normal duty cycle, the shovel positions itself against the working face without propel. In this situation, only the front-end assembly moves. Further, the maximum forces are involved during the excavation phase. Therefore, a dynamic model of the front-end assembly alone can suffice to describe the normal duty cycle of cable shovel. **Figure 3** shows the shovel front-end assembly, whose mechanism is modeled as a three-link system (saddle, crowd arm, and dipper) with three links and three joints. The saddle is a fixed length link and is free to rotate in the vertical plane. The rotation of the saddle block controls the vertical position of the dipper. The

crowd arm is connected to the saddle block through a prismatic joint, and its length varies during the crowding action of the digging operation.

The length of the crowd arm controls the horizontal position of the dipper. The crowd arm and the saddle have the same rotation cycle, while the dipper is oriented at a fixed angle, β, to the crowd arm. The dipper is also a fixed length link. The rotation of the saddle block and the length of the crowd arm together control the position of the dipper in the vertical plane and its trajectory. The structural kinematic parameters of the shovel using the Denavit-Hartenberg (D-H) notation [12] are represented in **Figure 3** and **Table 3**. Here, four values are assigned to each link following the D-H notation.
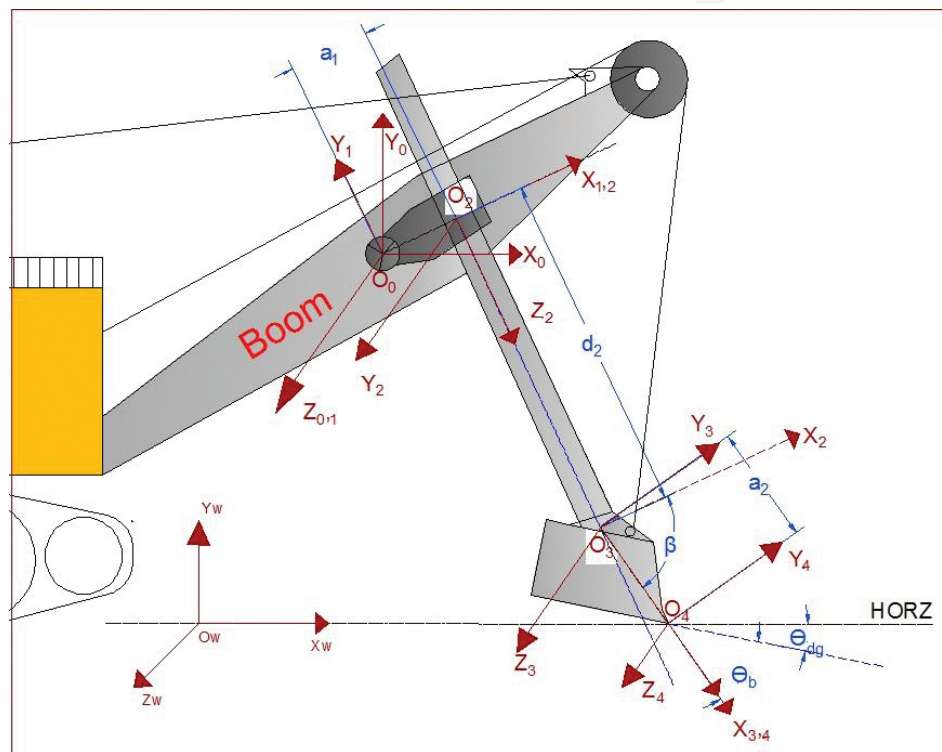

Figure 3. Structural kinematics using D-H procedure.

Link i	Joint description	α_i	a_i	d_i	θ_i
1	Saddle-boom joint	0	0	0	θ_1
2	Saddle-dipper handle joint	90	a_1	0	0
3	Dipper handle-dipper joint	−90	0	d_2	0

Table 3. Structural kinematic parameters.

The two values (a_i, d_i) are for the links and represent the constant and variable lengths of the links, while the other two (α_i, θ_i) are for the connection between links (i.e., joints), and, thus, represent the rotation of the coordinate frame and rotation of the joint, respectively. For a

revolute joint, ai, αi, and di are fixed and θi is a variable. On the other hand, for a prismatic joint (or translational motion), ai, αi, and θi are fixed and di is a variable. The crowd-arm movement is via a prismatic joint. A kinematic scheme relates the movements of the links and translates the motions and rotations in the reference coordinate frame. The D-H scheme is used to relate the movements and rotation of the links. The movements and rotations of individual links are measured in the coordinate frames assigned at every joint location using the D-H scheme [12]. The lower part of the shovel is stationary and fixed for this analysis.

The $X_oY_oZ_o$ frame, the reference coordinate frame, is selected with Z_o along the rotating axis of the saddle block. The coordinate frame $X_1Y_1Z_1$ coincides with the $X_oY_oZ_o$ frame and measures the rotation of the dipper handle via the saddle block. Next, the coordinate frame $X_2Y_2Z_2$ is set at the intersection of the saddle block and the dipper handle, with the Z_2 axis along the translation movement of the dipper handle (joint 2 being a prismatic joint). The movement of the dipper handle is measured along this Z_2 axis. The coordinate frame $X_3Y_3Z_3$ is set at the end point of the dipper handle with Z_3 normal to Z_2. This frame is at a fixed angle from coordinate frame 2. And finally, the frame $X_4Y_4Z_4$ is set at the tip of the dipper with Z_4-axis parallel to Z_3. The material resistive forces acting on the shovel are defined in this frame. The coordinate frame assignments are also shown in **Figure 3**.

Forward kinematics of cable shovel front-end assembly: The forward kinematic model defines the positions and motions of the dipper with known dipper-handle rotation and extension. External dynamic forces act on the shovel dipper during excavation. A transformation scheme is used to translate point coordinates in one coordinate frame to the first coordinate frame. The homogenous transformation matrix for transferring coordinates from *i−1* coordinate frame to *i* frame, in its general form for revolute and prismatic joints is given in Eqs. (2) and (3), respectively [13]. These equations can be derived considering two links (*i−1* and *i*) connected through revolute or prismatic joints, respectively. These transformation equations are a combination of rotation and translation matrices:

$$T_i^{i-1} = \begin{bmatrix} \cos\theta_i & -\cos\alpha_i\alpha_i\sin\theta_i & \sin\alpha_i\sin\theta_i & a_i\cos\theta_i \\ \sin\theta_i & \cos\alpha_i\cos\theta_i & -\sin\alpha_i\cos\theta_i & a_i\sin\theta_i \\ 0 & \sin\alpha_i & \cos\alpha_i & d_i \\ 0 & 0 & 0 & 1 \end{bmatrix} \tag{2}$$

$$T_i^{i-1} = \begin{bmatrix} \cos\theta_i & -\cos\alpha_i\alpha_i\sin\theta_i & \sin\alpha_i\sin\theta_i & 0 \\ \sin\theta_i & \cos\alpha_i\cos\theta_i & -\sin\alpha_i\cos\theta_i & 0 \\ 0 & \sin\alpha_i & \cos\alpha_i & d_i \\ 0 & 0 & 0 & 1 \end{bmatrix} \tag{3}$$

The individual transformation matrices T_i^{i-1} are formulated using Eqs. (2) and (3). These matrices relate the geometry of a point in the two adjacent coordinate frames as in **Figure 3** and can further be multiplied together to obtain a transformation matrix between any two coordinate frames. These transformations are required for the shovel front-end kinematic and dynamic models using the Newton-Euler procedure. The Newton-Euler method is an iterative method for computing the velocities, accelerations, joint torques, and forces from crowd arm

to dipper in the forward direction and from dipper tip to the saddle block in the reverse direction. Newton-Euler method has an advantage of being iterative, which makes it more suitable for computer simulations.

The propagation of angular and linear velocities from joint to joint is given by Eqs. (4) through (7) [13]. For rotational motion, the angular and linear velocities are defined by Eqs. (4) and (5), respectively. For prismatic joint, the angular and linear velocity relations are given by Eqs. (6) and (7), respectively:

$$^{i+1}\omega_{i+1} = {}^{i+1}_{i}R\ {}^{i}\omega_i + \dot{\theta}_{i+1}\ {}^{i+1}\hat{Z}_{i+1} \tag{4}$$

$$^{i+1}v_{i+1} = {}^{i+1}_{i}R\ ({}^{i}v_i + {}^{i}\omega_i\ X\ {}^{i}P_{i+1}) \tag{5}$$

$$^{i+1}\omega_{i+1} = {}^{i+1}_{i}R\ {}^{i}\omega_i \tag{6}$$

$$^{i+1}v_{i+1} = {}^{i+1}_{i}R\ ({}^{i}v_i + {}^{i}\omega_i\ X\ {}^{i}P_{i+1}) + \dot{d}_i\hat{Z}_i \tag{7}$$

The required rotation matrices are derived from the transformation matrices in Eqs. (2) and (3). The 3x3 matrix, within a transformation matrix T^{i-1}_i, represents the corresponding rotation matrix R^{i-1}_i. The forward kinematic starts from the first link (saddle block) and moves outward toward the last link (dipper). The objective is to determine the propagation of the joint rotation and velocities from the joint 1 to the dipper tip. The model uses the same start point equations and basic simplifying assumption from Frimpong et al. [14], and as a result, the kinematic equations are very similar as well. However, the resulting dynamic model is different due to the improved resistive forces in this model. The reference frame {0} is fixed with the lower frame through the boom. The lower structure of the shovel is fixed, so its linear and angular velocities and accelerations remain zero at all times during the excavation as shown in Eqs. (8) and (10). These values change only during the propel motion of shovel which is not considered in this research. The joint velocity can be determined by taking the derivative of rotation of joint 1 as shown in Eqs. (9) and (11), respectively. Similarly, the linear velocity of the stationary lower structure of the shovel is zero:

$$^{0}\omega_0 = \begin{bmatrix} 0 \\ 0 \\ 0 \end{bmatrix} \tag{8}$$

$$\frac{d\,{}^0\omega_0}{dt} = {}^0\dot{\omega}_0 = \begin{bmatrix} 0 \\ 0 \\ 0 \end{bmatrix} \tag{9}$$

$${}^0v_0 = \begin{bmatrix} 0 \\ 0 \\ 0 \end{bmatrix} \tag{10}$$

$$\frac{d\,{}^0v_0}{dt} = {}^0\dot{v}_0 = \begin{bmatrix} 0 \\ 0 \\ 0 \end{bmatrix} \tag{11}$$

Eq. (12) is obtained from Eq. (4) for joint 1 ($i = 0$), a revolute joint. It is evident from this equation that the angular velocity of the first link is only around Z-axis and is equivalent to the rate of change of angular rotation around joint 1. The linear velocity propagation to joint 1 can be computed using Eq. (5) as Eq. (13). The first link experiences only the rotational motion. Therefore, the linear velocity of joint 1 is zero:

$${}^1\omega_1 = {}^1_0R\,{}^0\omega_0 + \dot{\theta}_1\,{}^1\hat{Z}_1 = \omega_1 = {}^1_0R\,{}^0\omega_0 + \dot{\theta}_1\,{}^1\hat{Z}_1 = \begin{bmatrix} 0 \\ 0 \\ \dot{\theta}_1 \end{bmatrix} \tag{12}$$

$${}^1v_1 = {}^1_0R\,({}^0v_0 + {}^0\omega_0 \times {}^0P_1) = \begin{bmatrix} 0 \\ 0 \\ 0 \end{bmatrix} \tag{13}$$

For the prismatic joint 2 ($i = 1$), Eq. (6) computes the angular velocity of the link 2 (the crowd arm). The propagation of angular velocity to joint 2, as given in Eq. (14), shows that the angular velocity of joint 2 is dependent upon the rate of change of angular rotation of joint 1, and there is only an axis shift involved (from Z-axis to Y-axis) during the propagation:

$${}^2\omega_2 = {}^2_1R\,{}^1\omega_1 + \dot{\theta}_2\,{}^2\hat{Z}_2 = \begin{bmatrix} 0 \\ \dot{\theta}_1 \\ 0 \end{bmatrix} \tag{14}$$

$$\therefore \theta_2, \ \dot{\theta}_2, \text{and} \ \ddot{\theta}_2 \ are\ zero$$

$$^2v_2 = {}_1^2R\left({}^1v_1 + {}^1\omega_1 \text{ X } {}^1P_2\right) = \begin{bmatrix} 0 \\ 0 \\ -a_1\dot{\theta}_1 \end{bmatrix} \tag{15}$$

The linear velocity propagation to joint 2 is calculated as Eq. (15). Similarly, the angular and translational velocities are calculated for joint 3 as Eqs. (16) and (17). Again, the angular velocity of joint 3 is equivalent to the rate of change of angular rotation of joint 1. There is only one rotation of the joint involved for the front end during the digging cycle. Thus, the angular velocity of joint 4 is also the same as the angular velocity of joint 1. Alternately, it can be stated that the whole front-end assembly gets the same rotation as the joint 1 during the digging cycle, and the angular velocity only involves the axis shift. Eqs. (8) through (18) define the forward kinematics of the shovel front end. The angular and linear velocities of the shovel front-end components are defined using these equations with known initial rotation and crowd-arm extension:

$$^3\omega_3 = \begin{bmatrix} 0 \\ 0 \\ \dot{\theta}_1 \end{bmatrix} \tag{16}$$

$$^3v_3 = {}_2^3R\left({}^2v_2 + {}^2\omega_2 \text{ X } {}^2P_3\right) = \begin{bmatrix} d_2\dot{\theta}_1 \\ a_1\dot{\theta}_1 \\ 0 \end{bmatrix} \tag{17}$$

$$^4v_4 = {}_3^4R\left({}^3v_3 + {}^3\omega_3 \text{ X } {}^3P_4\right) = \begin{bmatrix} d_2\dot{\theta}_1 c_\beta + (a_1 + a_2)\dot{\theta}_1 s_\beta \\ -d_2\dot{\theta}_1 s_\beta + (a_1 + a_2)\dot{\theta}_1 c_\beta \\ 0 \end{bmatrix} \tag{18}$$

$$T_4^1 = \begin{bmatrix} c_\beta & -s_\beta & 0 & a_1 + a_2 c_\beta \\ s_\beta & c_\beta & 0 & a_2 s_\beta - d_2 \\ 0 & 0 & 1 & 0 \\ 0 & 0 & 0 & 1 \end{bmatrix} \tag{19}$$

Inverse kinematics of cable shovel front-end assembly: The inverse shovel kinematics determine the set of joint angles and the length for the crowd arm when the desired position and orientation of the shovel dipper are known in the reference coordinate frame 0. This inverse kinematic is useful when the dipper traverses a known trajectory to determine the joint rotation and crowd-arm extension required to achieve this trajectory. An approach, similar to the one used by Wu [15] for the reverse kinematic model of cable shovel, is used to determine the crowd-arm extension and rotation with known trajectory points. The inverse kinematic model can be achieved by coordinate transformations to obtain the dipper coordinate in coordinate frame

4, relative to coordinate frame 1. The modifications of the transformation matrix equations result in Eqs. (19), (20), and (21):

$$T_4^1 = \left[T_1^0 \right]^{-1} T_4^0 \tag{20}$$

$$T_4^0 = \begin{bmatrix} r_{11} & r_{12} & r_{13} & p_x \\ r_{21} & r_{22} & r_{23} & p_y \\ r_{31} & r_{32} & r_{33} & p_z \\ 0 & 0 & 0 & 1 \end{bmatrix} \tag{21}$$

The individual matrix elements are given as follows:

$$r_{11} : c_1 c_\beta - s_1 s_\beta;$$
$$r_{12} : -c_1 s_\beta - s_1 c_\beta;$$
$$r_{13} : 0;$$
$$r_{21} : s_1 c_\beta + c_1 s_\beta;$$
$$r_{22} : -s_1 s_\beta + c_1 c_\beta;$$
$$r_{23} : 0;$$
$$r_{31} : 0; \quad r_{32} : 0;$$
$$r_{33} : 0;$$
$$P_x : a_2 c_1 c_\beta - a_2 s_1 s_\beta + a_1 c_1 + d_2 s_1;$$
$$P_y : a_2 s_1 c_\beta + a_2 c_1 s_\beta + a_1 s_1 - d_2 c_1;$$
$$P_z : 0$$

Here, (p_x, p_y, and p_z) are the coordinates of the dipper tip in the reference coordinate frame 0. Eq. (22) can be derived from Eq. (2) and Eq. (23) from Eq. (20). Comparing the individual matrix elements on both sides of Eq. (23) and using simple arithmetic and trigonometric operations, the crowd-arm extension and rotation can be computed using Eqs. (25) and (26), respectively. The inverse kinematic model can be used to compute the positions and velocities of individual links and joints of the front-end assembly for a known trajectory:

$$\left[T_1^0 \right]^{-1} = \begin{bmatrix} c_1 & s_1 & 0 & 0 \\ -s_1 & c_1 & 0 & 0 \\ 0 & 0 & 1 & 0 \\ 0 & 0 & 0 & 1 \end{bmatrix} \tag{22}$$

$$\begin{bmatrix} - & - & - & c_1 p_x + s_1 p_y \\ - & - & - & -s_1 p_x + c_1 p_y \\ - & - & - & p_z \\ - & - & - & 1 \end{bmatrix} = \begin{bmatrix} c_\beta & -s_\beta & 0 & a_1 + a_2 c_\beta \\ s_\beta & c_\beta & 0 & a_2 s_\beta - d_2 \\ 0 & 0 & 1 & 0 \\ 0 & 0 & 0 & 1 \end{bmatrix} \tag{23}$$

$$d_2 = a_2 s_\beta + \sqrt{p_x^2 + p_y^2 - a_1^2 - a_2^2 - 2a_1 a_2 c_\beta + \left(a_2 s_\beta\right)^2} \tag{24}$$

$$\theta_1 = A\tan 2\left(a_2 s_\beta - d_2, \pm\sqrt{p_x^2 + p_y^2 - \left(a_2 s_\beta - d_2\right)^2}\right) - A\tan 2(p_y, p_x) \tag{25}$$

4. Dynamic model of the cable shovel front-end assembly

The dynamic model defines forces and torques acting on the shovel links and joints from the kinematics parameters, such as accelerations. The forces require the computation of angular and linear accelerations, which can be obtained by time integration of the angular and linear velocities computed in the kinematic model. In its general form, the dynamic model can be defined as in Eq. (26) from Frimpong et al. [16]:

$$\begin{aligned} D(\Theta)\ddot{\Theta} + C\left(\Theta, \dot{\Theta}\right)\dot{\Theta} + G(\Theta) &= F - F_{load}(F_t, F_n) \\ D(\Theta) &= \text{mass matrix} \\ C\left(\Theta, \dot{\Theta}\right) &= \text{centrifugal and Coriollis terms} \\ G(\Theta) &= \text{gravity terms} \end{aligned} \tag{26}$$

This dynamic model for a shovel is built using the Newton-Euler method and the position, velocity, and acceleration relationships computed from the kinematic model. The Newton-Euler dynamic algorithm for computing the crowd force and the hoist torque comprises of the following steps:

1. Compute the angular acceleration $(\dot{\omega}_i)$ of every link in the forward direction, starting from the saddle and moving outward toward the last link (the dipper).

2. Compute the acceleration $(\dot{v}_i)$ of every link in the system in the forward direction.

3. Compute the acceleration $(\dot{v}_{ic})$ at the left of mass (centroid) of every link in the system in the forward direction.

4. Determine the force (F_i) acting on every link at the centroid of the link using (v_{ic}) and mass of the link.

5. Compute the joint torque (N_i) for every link.

The force and torque are computed at the centroid of each link. Therefore, the velocity and the acceleration of the centroid are computed for every link.

5. Numerical modeling and simulation of the dipper-formation interaction

The dynamic model is a system of ordinary differential equations (ODEs), which results from an iterative process and includes a number of ODE subprocesses. The ODEs are numerically solved in MATLAB using the embedded Runge-Kutta algorithm. The simulation model consists of MATLAB programs (.m files) and SIMULINK design-based models and sub-models. The simulation model consists of the main model and sub-models. These sub-models define the dipper's trajectory, the crowd-arm extension and rotation, and the resistive forces (cutting forces, material, and dipper's weight) on the dipper. The following sub-models and main model are created:

1. *Test bench geometry and trajectory*: **Figure 4** shows the test bench geometry created for the digging process simulation. The excavated material characteristics can be selected for various digging conditions. A simulation step size is selected to make the dipper move with a constant linear velocity following field experimental results [17]. The failure surface is modeled as a quadratic function given by Eq. (27), and bench face is modeled as a straight-line function L(x). During the simulation process, the coordinates of the dipper tip ($O_4(x,y)$) and the dipper depth into the working bench (d) are continuously computed at every time step using Eqs. (28) and (29), respectively:

$$y = 0.9927x^2 - 22.557x + 117.68 \tag{27}$$

$$O_4x, y = \left[-0.4837t^2 + 2.4351t + 12.053, \qquad 0.9927 * x^2 - 22.557 * x + 117.68 \right] \tag{28}$$

$$d = O_4(x) - L(x) \tag{29}$$

2. *Crowd-arm extension and rotation angle*: This sub-model calculates the extension and rotation of the crowd arm at every simulation step using Eqs. (24) and (25).

3. *Payload and force f_1*: The payload forms the basis for the dynamic payload force (f_1). **Figure 4** defines the dipper trajectory in such a way that the dipper is filled as it leaves the bank without any material spillage. At any instant, therefore, the payload is equivalent to the area between the trajectory curve and bench face.
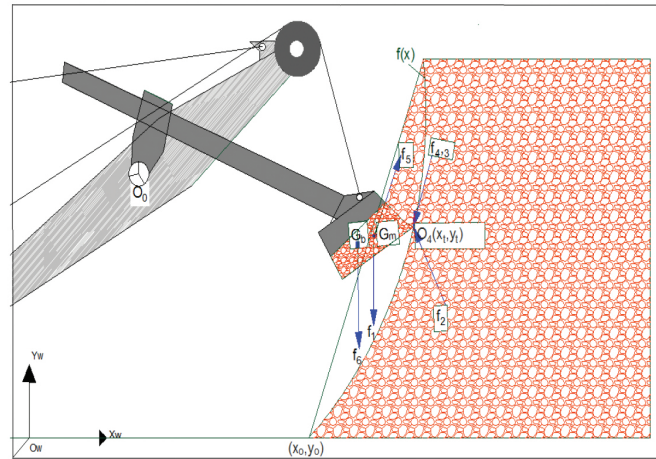

Figure 4. Representative bench geometry.

At each simulation step, the (x, y) trajectory coordinates and the area excavated (A_c) are numerically computed using Eq. (30) [8] and built-in routines in MATLAB R2012a. This area is used to calculate the force (f_1) due to the payload weight using Eq. (31) [8]. An optimization algorithm [8] is used to define the geometry of the payload based on the material distribution from Hemami [6]. The centroid of each material geometry, a polygon inside the dipper, is computed using a special algorithm [18]. This centroid is a dynamic point, which is used as the point of application for the dynamic force f_1. This force (f_1) is computed continuously at every instant of the excavation process:

$$A_c = \frac{1}{2}(x_t - x_o)^2 \tan\alpha - \int_{x_o}^{x_t} f(x)dx \tag{30}$$

$$f_1 = A_c \omega \rho g \tag{31}$$

4. *Material resistive force f_6*: The force, due to the weight of the dipper, is calculated during the digging cycle along the trajectory. The computation of centroids of payload geometry and dipper suggests that these two centroids can be considered concentric. Therefore, both f_1 and f_6 are combined into single force acting at the dynamic left of the payload geometry.

5. *Digging resistive forces f_3 and f_4*: The resistive forces, f_3 and f_4, are combined as a single cutting force (F_r) and calculated using Eq. (1) [11]. The cutting force (F_r) acts along the tangent of the trajectory at the dipper tip. This force is resolved into its rectangular components, one along the dipper base and the other normal to it. These tangent and normal components (F_t and F_n) of the resistive force (F_r) are computed at every trajectory point in this sub-model.

6. *The main model and numerical simulation*: The dynamic model of the dipper-teeth assembly is solved in the main model. The outputs from all the sub-models, along with system constants and time steps are fed into the main model as inputs. The main model then numerically solves the mathematical model and generates the desired outputs. Two of the important results or outputs from this solution are the hoisting force (F_1) and crowd-arm torque (T_1).

During this numerical simulation process, four of the six resistive forces (f_1, f_3, f_4, f_6) are computed as separate subsystems, while the other two resistive forces (f_2 and f_5) are set to zero. The resistive force f_2 is set to zero by selecting an appropriate trajectory of the dipper [6]. The excavation trajectory is selected in such a way that the dipper stays clear off the material and does not compress the material. This assumption is reasonable in the sense that it involves proper bench geometric design and operator skill. An improper bench geometric design would lead to undue stresses on the shovel, which must be avoided during the excavation process. The force f_5 represents the dipper and payload inertia. This force can be set to zero if the dipper moves through the material with a constant velocity and hence with zero acceleration. For this research, it is assumed that the dipper moves through the bench with a constant velocity and hence a zero acceleration. This assumption is consistent with the field observations [17] for hoist rope extension.

6. Virtual shovel prototype simulation

A virtual 3D prototype of the rope shovel is built in AutoCAD-2012 as shown in **Figure 5**. The dimensions of the shovel front-end assembly are chosen to represent the dimensions of the P&H 4100XPC shovel and are measured from a scaled model [19]. The front-end geometry is simplified to avoid unnecessary geometric complications. The model consists of one revolute and two prismatic joints that control the motion of the dipper into the formation. The boom and saddle are modeled as rigid bodies. The boom is considered fixed to the ground. Both joints are constrained; the revolute joint allows rotation only in the z-axis, and the prismatic joints allow motion only in the x-axis. The resistive forces of the formation are applicable as a remote force available at the teeth. The material force is also modeled as a remote force acting on the dipper. The revolute joint is given a fixed rotation at every time step to ensure the completion of the digging cycle in 3 s. The contacts and boundary conditions are shown in **Figure 6**. The dipper body is modeled using brick elements with a minimum of three elements through the thickness of the dipper.

The dipper trajectory is given as an input function to the shovel simulation process in MAT-LAB/SIMULINK. The dipper traverses the known trajectory, and the reverse kinematic model is used to determine the crowd-arm extension (d_2) and rotation (θ_1) requirements to achieve this trajectory. These two output parameters from the numerical simulation process are used as inputs for the shovel prototype. Together, these two inputs define the dipper trajectory. Similarly, the resistive forces computed during the shovel dynamic simulation are modeled as higher order polynomial in MATLAB and are fed into the system as time functions. The payload also exerts a force on the dipper side walls. This force is modeled using the earth pressure at-rest theory [20] and is considered to be acting uniformly over the side wall.
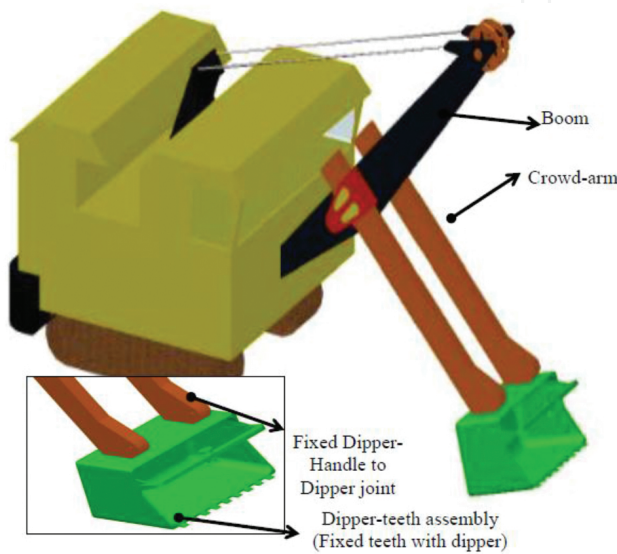

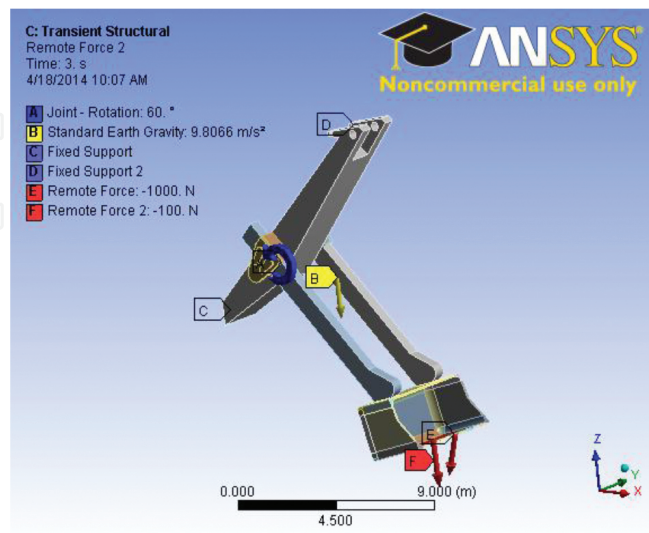
Figure 5. Simplified 3D model of cable shovel and dipper.

Figure 6. Boundary conditions and external forces on shovel front end.

7. Shovel stress modeling and analysis

The steel used for cable shovel dippers and teeth has high strength properties. The yield strength is the most important strength property, as the shovel experiences high levels of stress loading. Limited data is available for shovel components [21]. One research reported csa-g40.21-350WT steel used for shovel boom [21]. This steel has high yield strength of 320 MPa [21, 22]. It is assumed in this study that the same steel is used for the dipper and the shovel boom, and their properties are given in **Table 4**. The angular rotation and extension of the dipper arm, external digging forces, and dynamic material weight forces from the dynamic simulated model are used as inputs for the virtual prototype. The shovel stress analysis is performed in ANSYS Workbench-R15.0 [30]. First, a rigid-body analysis is performed to ensure that the dipper follows the given trajectory for the given angular rotation, crowd-arm extension, and external forces. Afterward, a transient analysis is performed for the dipper and teeth stress analysis in ANSYS Workbench R15. For this analysis, the dipper-teeth assembly and crowd arm are converted into flexible bodies, allowing ANSYS to compute stresses on the dipper components. All force functions are the same as that used for the rigid-body analysis. The joint functions are defined for the desired trajectory generation. The flexible dipper bodies are meshed appropriately, using sweepable bodies and controlled meshing. The simulations are performed for a 3 s interval. The simulation is run in two steps with multiple sub-steps for better convergence.

Property	Value	Unit
Density	7900	kg/m^3
Young's modulus	2.3E+11	Pa
Poisson's ratio	0.3	
Tensile yield strength	3.2E+08	Pa
Compressive yield strength	3E+08	Pa
Tensile ultimate strength	4.6E+08	Pa

Table 4. Properties of steel for dipper and teeth.

Stress loading (von Mises) is computed for the dipper-teeth assembly, dipper bottom plate, dipper side wall, and teeth. **Figure 7** shows the representative stress profile. The stresses on the dipper-teeth assembly vary with time. The maximum stress values vary from 151 MPa to 282 MPa. These stress values are higher than the lower limits of yield strengths for low, medium, and high carbon steel (**Table 5**). Permanent damage to the dipper components is possible, if the steel used has lower yield strength. The stress contour maps are used to identify the high and lower stress regions for fatigue fracture modeling and analysis.
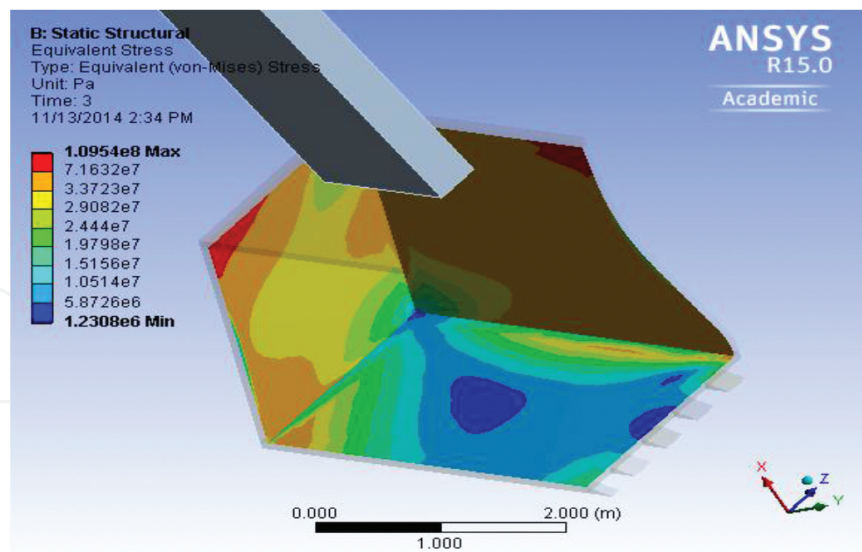
Figure 7. Equivalent stress (von Mises) profile of dipper.

Steel	Yield strength [MPa]
Low carbon steel	140–2400
Medium carbon steel	245–1740
High carbon steel	375–3340

Table 5. Yield strengths of steel [23].

8. Fatigue failure modeling of dipper components

Rope shovel excavation is cyclic in nature. The stresses on the front-end assembly vary continuously during the duty cycle [24]. This variation, combined with the material flaws, can initiate fatigue cracks in shovel components. Environmental factors (e.g., freezing temperatures and corrosive materials) affect metal toughness. Fatigue crack may grow rapidly to undesirable lengths under cyclic loading conditions. There are three modes for metal fatigue failure: (i) mode-I (crack opening), (ii) mode-II (in-plane shear or crack opening), and mode-III (out-of-plane shear or crack twist). Metal failure can also be a result of mixed-mode fatigue. Mode-I fatigue research has dominated the fatigue analysis and life-expectancy field. Three common fatigue failure analysis approaches are typically used, including the stress life, strain life, and fracture mechanics. Each approach has its own application with overlapping boundaries. The fracture mechanics approach is used to estimate a crack's propagation life. For this approach, the initial crack lengths are either assumed or known (welds, known defects, porosities, and cracks found during nondestructive testing). Fracture mechanics principles and theories are applied to estimate crack-propagation rates and, thus, crack-propagation lives.

A typical crack-growth curve has three distinct regions: crack initiation, crack propagation, and rapid increase in crack growth leading to failure. Fatigue life may, however, occur for a longer period of time during the crack-propagation phase as the majority of crack time is spent during this phase. A number of models are available to predict the crack-propagation phase (the middle region on the curve). Paris' law [25], defined by Eq. (32), is the most commonly used method to estimate the crack propagation. The slope of the linear region of the fatigue curve defines the crack-growth rate with every cycle. The material constants (C, m) can be found for different metals in literature or computed using standard tests (ASTM E647):

$$\frac{da}{dN} = C(\Delta K) \tag{32}$$

K is the stress intensity factor (SIF). According to the linear elastic fracture mechanics (LEFM) theory, computation of stress intensity factor (SIF) at the crack tip is necessary to predict the crack growth. SIFs for many simple geometries and loading situations are available in published literature [26–29]. For complex geometries and stress loading conditions, numerical methods are used to compute the reliable SIF values. The most common methods for calculating SIF are the J-integral and energy release rate. Finite element techniques evaluate the SIF using the energy release rate method. Many commercial software packages, such as ANSYS Workbench (R15), have options for calculating these parameters. In these techniques, energy release is estimated around the crack tip nodes in close loops, in the form of contours. For 2D cases, the node at the crack tip forms the first contour, while for 3D cases, all nodes forming the crack front determine the first contour. The shape, length, and depth of a crack determine the crack life at a specific location.

For fracture modeling of the dipper, representative cracks can be induced in the virtual shovel. **Figure 8** illustrates the location and geometry of an elliptical crack in the dipper's bottom plate. The crack is induced in the high stress region and is along the stress lines. This representative crack is 3 in. long and is 1 in. deep. A localized reference system defines the geometry of this crack. The crack plane lies on this XZ plane, while the width of crack is along the Y direction of this plane. The crack grows along the X and Z directions. A number of parameters control the crack failure modeling, including crack geometry, shape, orientation, and stress environment. The crack definition is explained in **Figure 9**. This crack front is divided into a number of segments, and six circular contours (also divided into segments) are generated around the crack front. All these divisions represent the node locations for the finite element model. The J-integral values are computed for every contour along the crack front. These values are used to compute the SIFs at the crack tip and for life estimations.

The crack size is the most critical aspect of fatigue crack modeling and dipper life estimation. The SIFs are highly dependent upon the crack size (length and depth). The relationship between SIF and crack length is nonlinear. Estimating the variation of SIFs with size is the most important and critical aspect for life estimation. The experimentation is performed for multiple size cracks. ANSYS R15 software is used to compute the J-integrals around the predefined crack tips. As explained in **Figure 9**, contours are generated around the crack front to represent

the closed paths for J-integral. There are six contours around every modeled crack as illustrated in **Figure 10**. A very fine mesh size is generated around the crack tip, and J-integrals are computed for all these contours. The first contour is very close to the tip and may represent erroneous results. Therefore, the J-integral values for the first contour are ignored to ensure accuracy [30].
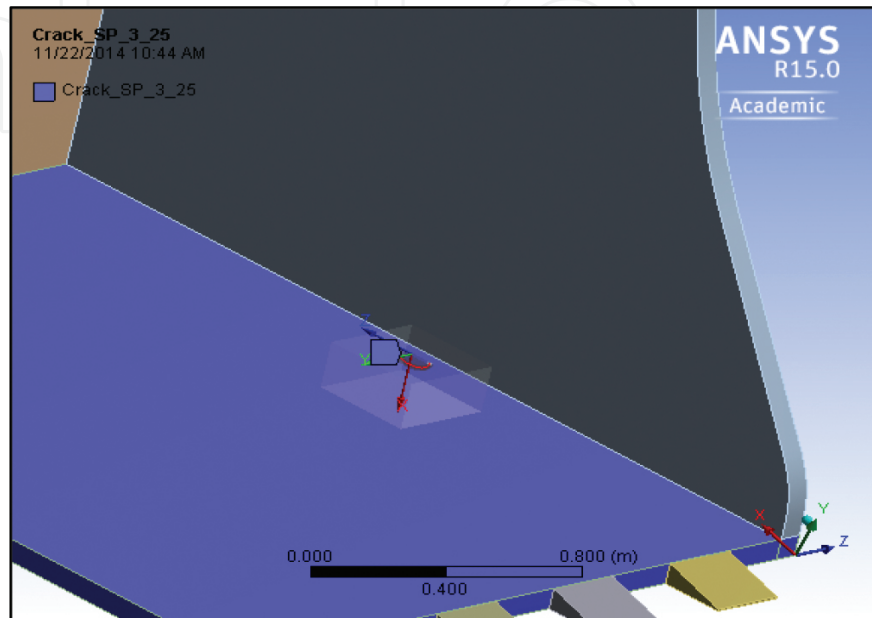

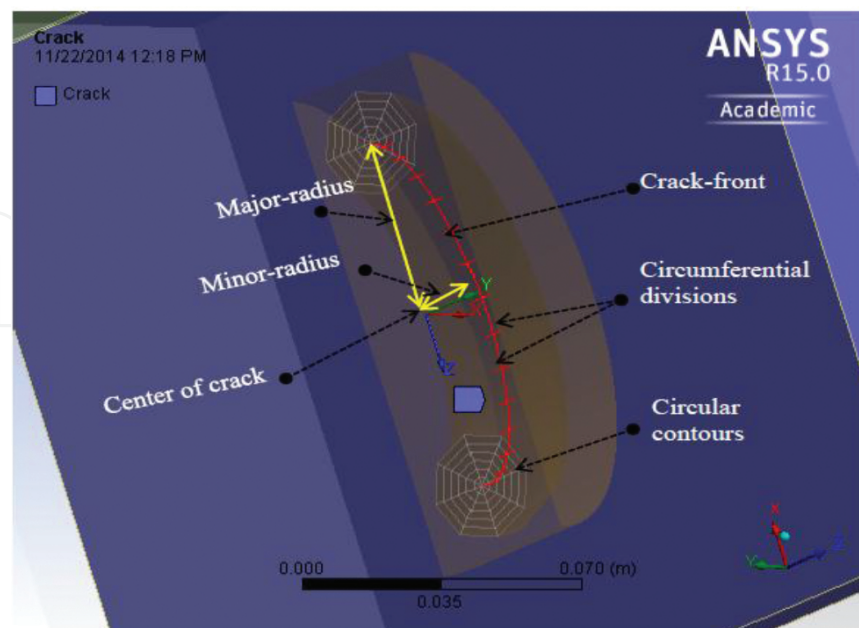**Figure 8.** Elliptical crack at the side of the dipper bottom plate.

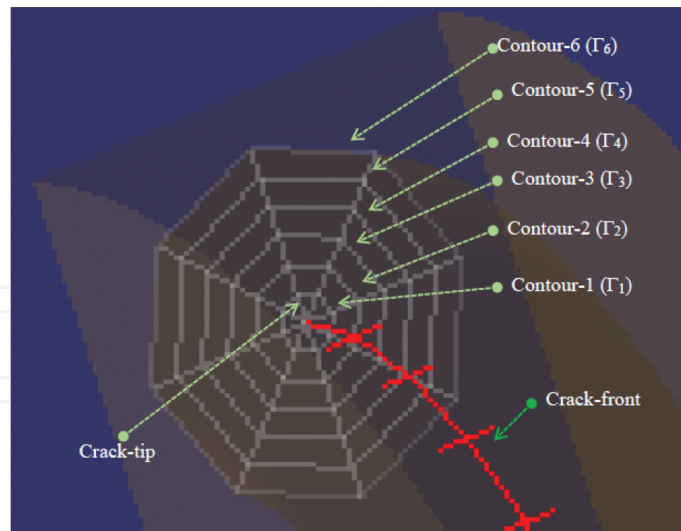**Figure 9.** Crack definition in ANSYS for J-integral computations.

Figure 10. ANSYS contours for J-integral computations.

SIFs are computed, using plane stress conditions for all the contours, and an average value of five contours (contour 2–6) is used for further fatigue analysis. Crack lengths are increased from smaller to larger crack sizes at selected locations, and SIFs are computed for each crack size. The results are used to generate the crack-growth curves and for life expectancy of dipper components. The SIF variation curves for the bottom-plate crack tip are obtained through a least square regression and curve fitting process, Eq. (33), and are plotted in **Figure 11**. The crack is in a high stress region, and, thus, the SIF is very high. Further, the SIFs show a steep increase with crack size. It is expected that the cracks at this location will propagate rapidly:

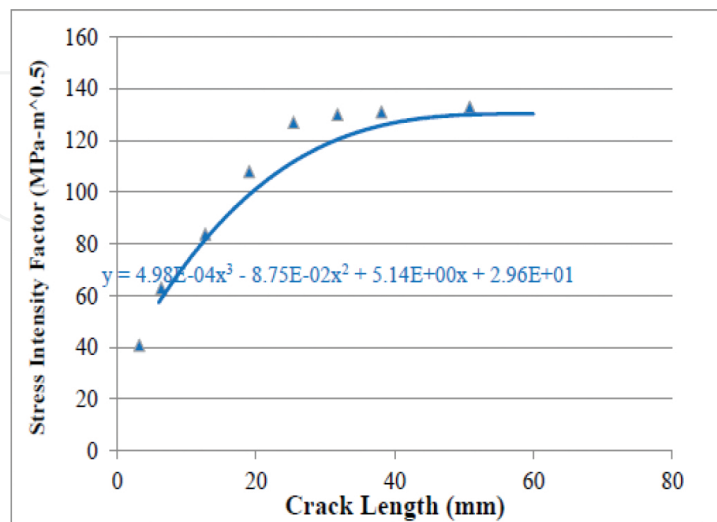$$SIF = 4.98E - 04a^3 - 8.75E - 02a^2 + 5.14a + 2.96E + 01 \tag{33}$$

Figure 11. SIFs for the bottom-plate crack tip.

9. Remaining life expectancy of dipper components

Fatigue life is modeled by integrating the Paris' law [25] in Eq. (34). The equation has three input parameters (c, m, and ΔK). The two material constants are computed following standard laboratory procedures. For common materials, the values for these variables can also be found in literature [31, 32]. The "c" values are between 3 and 4, and some common values for "m" are available in literature [33]. For this research, the material constants are taken from research conducted by Yin et al. [21, 22]. They estimated the crack growth for the shovel boom cracks and measured the material constants ("c" and "m") following the ASTM standard E1820:

$$N_f = \int_{a_i}^{a_f} \frac{da}{m(\Delta K)^c} \tag{34}$$

It is also assumed that the steel properties for the dipper and teeth are similar to that for the boom. With these parameters, Eq. (34) becomes Eq. (35). As the computations become complex, it is numerically solved using Gauss-Legendre quadrature in MATLAB. The outputs from Eq. (35) include number of cycles (N_f) for a crack to propagate from an initial length (a_i) to a final length (a_f). The number of cycles is converted to number of days assuming that one digging cycle of shovel is equivalent to one fatigue cycle:

$$N_f = \int_{a_i}^{a_f} \frac{da}{5.89^{-12}(\Delta K)^{3.27}} \tag{35}$$

Following the Palmgren-Miner's rule [34] for equivalent damage, the total number of fatigue cycles per day is equal to the digging cycles of the shovel per day. The total number of cycles for a shovel per day is counted using the cycle time and the operational efficiency. The shovel digging cycle is assumed to be 3 s for this research. However, a typical complete excavation cycle time for P&H 4100XPC is about 30 s. The 3 s cycle time is consistent with the numerical simulation results. Using this cycle time and assuming a 95% shovel operational efficiency, the total number of digging cycles for shovel is calculated as 2730 cycles per day. This assumption is very close to field observations [22] where researchers counted 2880 cycles per day for a cable shovel working continuously over a period of 2 weeks. For this research, a middle-ground value of 2800 cycles per day is assumed to convert the cycles to days.

The remaining useful life for the cracked components can be estimated, with knowledge of critical crack lengths for dipper material. The critical crack length is the length of the crack at which the material at the crack tip starts behaving like a plastic material, and the crack propagation becomes very rapid. It is represented as the boundary between the second and third zones for a fatigue crack. The critical lengths for metals are generally measured using laboratory fatigue toughness tests following the standard procedures. A critical length limit

may also be implemented based on field operating conditions or using the crack-growth curves.

The crack-growth curve for the dipper bottom plate is shown in **Figure 12**. It is observed that the crack-propagation rates become very high after a certain crack length. A critical length[1] of 100 mm is set for this crack. As illustrated in this figure, the estimated life for a 50 mm bottom-plate crack is 38 days. However, once the crack grows to 75 mm, the remaining life is only 16 days for the same crack.
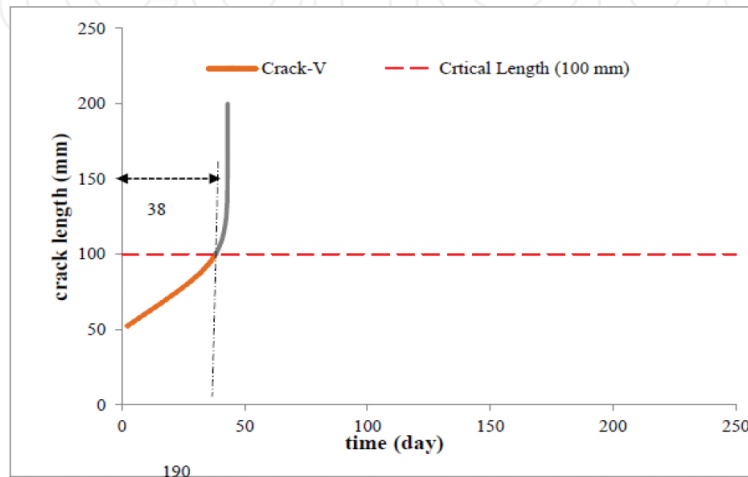

Figure 12. Critical crack length and remaining life expectancy for an initial length of 50 mm.

10. Significant contributions

The research underlying this chapter is a pioneering effort for understanding electric rope shovel dipper stress analysis using dynamic resistive forces. The research results contribute to the existing body of knowledge on health and longevity of shovel dipper-teeth assembly. It advances shovel reliability, maintainability, and availability, which influence surface mining productivity. Previous research generally ignored the dynamic forces due to the weight of the dipper and payload. Given the size of current large shovels with 100+ tons per pass, these forces must be accounted for in any meaningful and comprehensive dynamic model. The research models provide detailed information on the forces and torques for all joints and links within the shovel front-end assembly. This research is also the first attempt to model the fatigue life of the shovel dipper-teeth assembly. It lays a foundation for understanding dipper fatigue failure resulting from high stress intensity, crack initiation, and propagation for rope shovel front-end assembly. Research shows that dipper-related breakdowns are among the highest for shovel excavation downtimes [4]. The current maintenance practice for the shovel front-end assembly is based on experience rather than science. This chapter lays a foundation for

---

[1] Crack length in this text (and in literature) is always referred as half of the total length of crack. A critical length of 100 mm would be 200 mm total length of the crack.

the scientific modeling and understanding of the shovel dipper-teeth stress and fatigue failure studies. The life expectancy of the shovel components should help reduce the operating costs of shovel excavation. Overall, the study contributes to the health and longevity of the large rope shovels by providing a more scientific basis to the subject matter and should be helpful in the design and development of the next generation of excavators. The results of these models can be used to design and build the next generation of shovel dippers for the surface mining industry and advance frontiers and knowledge in shovel dipper stress and fatigue failure modeling.

11. Conclusions

Estimating electric rope shovel health and longevity is a complicated task and requires a thorough understanding of the shovel digging process. Thus far, the shovel front-end assembly repair model is based on experience and judgment rather than science. Shovel kinematic and dynamic models provide a scientific basis for shovel repair and fatigue failure modeling. The shovel dynamic model requires a good estimation of shovel digging forces. Current rope shovels have large dipper capacities, and their digging resistive forces can be significant. Shovel payload is a dynamic and significant contributor of these digging forces. The dynamic forces result in stress loading of shovel front-end components. The maximum stress values can be as high as 282 MPa and can be higher than the lower yield strength limits for low, medium, and high carbon steel. Material flaws, high stresses, and other environmental factors can initiate cracks on the dipper. Under severe stress loading conditions, these cracks can propagate to critical lengths in no time. The estimated life for a 50 mm bottom-plate crack was found to be 38 days. However, once the crack grows to 75 mm, the remaining life can be as low as 16 days only. This chapter lays a foundation for the fatigue failure analysis of dipper-teeth assembly. The virtual prototype is a scaled and simplified model. It is recommended that the work be extended for real full-scale virtual prototype for the actual steel materials used.

Nomenclature

C_o number of impacts to sink a cylindrical tip in a standardized test by 10 cm

ϱ the angle that the rupture surface makes with the horizontal

β tool cutting angle for Zelenin model

d tool working depth, depth of dipper into the bench

w width of tool

z coefficient for teeth configuration in the Zelenin model [11]

w dipper width

da/dN crack-growth rate per cycle as defined by Paris' law

a   crack length

N_f number of cycles to failure

K   stress intensity factor

C, m   material constants for Paris' law

a_i, a_f initial and final/critical known/assumed crack length

$C(\Theta,\bar{\Theta})$ generalized Coriolis and centripetal torque

$D(\Theta)$ generalized inertia matrix

$G(\Theta)$ generalized gravity torque

m_1, m_2 mass of crowd arm and dipper, respectively

αi rotation of coordinate frame with respect to i−1 frame

β constant inclination of link 3 from link 2 (inclination of X_4 from X_3)

θ_i rotation of ith coordinate frame

θ inclination of coordinate frame {4'} from coordinate frame 3

a_i length of the ith link

a_1 crowd-arm length from pivot to connection point between arm and dipper (length of 1st link)

a_2 length between dipper tip and connect point of arm and dipper (length of second)

s_i, c_i $\sin\theta_i$ and $\cos\theta_i$, respectively

di   offset distance of the gravity left in link i

F_n, F_t normal and tangential cutting resistive forces on dipper tip

$^{i+1}T_i$ transformation matrix to transfer the coordinates from i to i+1

$^{i+1}R_i$ rotational matrix, extracted from $^{i+1}T_i$

$L(x)$ straight-line function representing the bench face

Author details

Muhammad Azeem Raza[1] and Samuel Frimpong[2*]

*Address all correspondence to: frimpong@mst.edu

1 University of Engineering and Technology, Lahore, Pakistan

2 Missouri University of Science and Technology, Rolla, USA

References

[1] Caterpillar. *Electric Rope Shovels*. 2012 [cited 2012]; Available from: https://mining.cat.com/products/surface-mining/electric-rope-shovels.

[2] P&H. *P&H Mining Equipment*: *Electric Rope Shovels*. 2011 [cited 2011 March 10, 2011]; Available from: http://www.phmining.com/en/PHMining/Mining-Equipment/Electric-Shovels/4100XPC.htm.

[3] Roy, S.K., M.M. Bhattacharyya, and V.N.A. Naikan, *Maintainability and Reliability Analysis of a Fleet of Shovels*. Transactions of The Institution of Mining & Metallurgy, 2001: A163–A171.

[4] S. K. Roy, M. M. Bhattacharyya & V. N. A. Naikan (2001) Maintainability and reliability analysis of a fleet of shovels, Mining Technology, 110:3, 163-171, DOI: 10.1179/ mnt. 2001.110.3.163

[5] Lipsett, M.G. and Y.R. Moghaddam, *Bifurcations, Instabilities and Degradation in Geomaterials*, *SSGG*, in *Modeling Excavator-Soil Interaction*; W. Richard, M.Alsaleh, LabuzJoe, Editor. 2011, Springer.com: 347–366.

[6] Hemami, A., *An Approximation of the Weight of the Loaded Material During the Scooping Operation of a Mechanical Loader*. Transactions of the Canadian Society of Mechanical Engineering, 1994. 18(3): 191–205.

[7] Hemami, A., S. Goulet, and M. Aubertin, *Resistance of Particulate Media to Excavation*: *Application to Bucket Loading*. International Journal of Surface Mining, Reclamation and Environment, 1994. 8(3): 125–129.

[8] Awuah-Offei, K., S. Frimpong, and H. Askari-Nasab, *Formation Excavation Resistance Modeling for Shovel Dippers*. International Journal of Mining and Mineral Engineering, 2009. 1(2): 127–146.

[9] Takahashi, H., M. Hasegawa, and E. Nakano, *Analysis on the Resistive Forces Acting on the Bucket of a Load-Haul-Dump Machine and a Wheel Loader in the Scooping Task*. Advanced Robotics, 1999. 13(2): p. 97–114.

[10] Balovnev, V., I, *New Methods for Calculating Resistance to Cutting of Soil*. 1983: Amerind, New Delhi, India.

[11] Zelenin, A.N., V.I. Balovnev, and I.P. Kerov, *Machines for Moving the Earth*. 1985: Amerind, New Delhi, India.

[12] Koivo, A.J., *Fundamentals for Control of Robotic Manipulators*. 1989: Jhon Wiley & Sons, Inc. New York, NY, USA

[13] Craig, J.J., Introduction to Robotics: Mechanics and Control. 2nd ed. 1996: Prentice Hall, Upper Saddle River, New Jersey, USA.

[14] Frimpong, S., Y. Hu, and K. Awuah-Offei, *Mechanics of Cable Shovel-formation Interactions in Surface Mining Excavations*. Journal of Terramechanics, Elsevier Ltd., New York, NY 2005: p. 15–33.

[15] Wu, H., *Modeling and Simulation of Electric Mining Shovels*, in *Department of Mining and Metallurgical Engineering*. 1995, McGill University, Montreal, Quebec, Canada.

[16] Frimpong, S., Y. Hu and H.I. Inyang. Dynamic Modeling of Hydraulic Shovel Excavators for Geomaterials. International Journal of Geomechanics. 2008 Vol. 8(1), ASCE, Reston, VA: 2–10.

[17] Hendricks, C. and M. Scoble. *Post-Blast Evaluation Through Shovel Performance Monitoring*. In *Proc. of the Conference on Explosive and Blasting Technique*. 1990, © ISEE, Orlado, FL.

[18] Sommer H.J., *POLYGEOM.m*: *Geomery of a Planar Polygon*. 2011.

[19] P&H. *4100XPC Electric Mining Shovel*. 2012 [Sep, 30, 2012]; Available from: http://www.minepro.com/MinePro/Literature/Spec/4100XPC-AC.pdf.

[20] Coulomb, C.A., *Essai Sur Une Application Des REgles Des Maximis et Minimis a Quelques Problems de Statique Relatifs a l'architechture*. Academic Royale des Sciences: Memories de Mathmatique et de Physique, presentes a l'Acaemie Royale des Sciences, par Divers Savants, Paris, 1776. 7: 343–382.

[21] Yin, Y., et al., *Fatigue life prediction of heavy mining equipment. Part 2*: *Behaviour of corner crack in steel welded box section and remaining fatigue life determination*. Journal of Constructional Steel Research, 2008. 64(1): 62–71.

[22] Yin, Y., et al., *Fatigue life prediction of heavy mining equipment. Part 1*: *Fatigue load assessment and crack growth rate tests*. Journal of Constructional Steel Research, 2007. 63(11): p. 1494–1505.

[23] matweb. *Material Property Dataseet*. 2014 [cited 2014 12/2/2014]; Available from: http://www.matweb.com/search/QuickText.aspx?SearchText=carbon%20steel.

[24] Frimpong, S. and Y. Hu, *Intelligent Cable Shovel Excavation Modeling and Simulation*. International Journal of Geomechanics (c) ASCE, 2008. 8(1): p. 2–10.

[25] Paris, W.G. and F. Erdogan, *A Critical Analysis of Crack Propagation Laws*. Trans. of ASME. Journal of Basic Engineering, 1963. D85: p. 528–534.

[26] Loakimidis, N.I. and P.S. Theocaris, *The Numerical Evaluation of a class of generalized stress intensity factors by use of the Lobatto-Jacobi numerical integration rule*. International Journal of Fracture, 1978. 14: p. 469–484.

[27] Raju, I.S. and J.C. Newman, Jr., *Three Dimensional Fine-Element Analysis of Finite-Thickness Fracture Specimens*. NASA Langely Research left, United States., 1997: p. 42.

[28] Sih, G.C., *Handbook of stress-intensity factors*. 1973: Lehigh Univ., Institute of Fracture and Solid Mechanics. Bethlehem, Pennsylvania, USA.

[29] Tada, H., Paris, P.C. and G.R. Irwin, *Stress Analysis of Cracks Handbook*. 1973: Del Research Corp., Hellertown, PA.

[30] ANSYS, *ANSYS Workbench Help Documentation*. 2014, ANSYS Inc. Southpointe 275 Technology Drive Canonsburg, PA, USA.

[31] Chapra, S.C. and R.P. Canale, *Numerical Methods for Engineers: with PC Applications*. 1985: McGraw-Hill, NY.

[32] Rolfe, S.T. and J.M. Barson, *Fracture and Fatigue Control in Structures*. 1977: Prentice-Hall, Englewood, NJ.

[33] Throop, J.F. and G.A. Miller, *Optimum Fatigue Crack Resistance Acheivment of High Fatigue Resistance in Metals and Alloys, ASTM STP 467*. 1970: American Society for Testing and Materials, Philadelphia.

[34] Miner, M.A., *Cummulative Damage in Fatigue*. Journal of Applied Mechanics, 1945. 67.